Nanoscale

ROYAL SOCIETY OF CHEMISTRY

PAPER

View Article Online
View Journal | View Issue

Check for updates

Cite this: *Nanoscale*, 2026, **18**, 336

Surface dependent organometallic to covalent transition in graphdiyne molecular wires

Alice Cartoceti,[a] Simona Achilli,*[b,e] Paolo D'Agosta,[a] Francesco Tumino,[a] Shreya Garg,[c] Alessio Orbelli Biroli,[d] Giovanni Onida,[b,e] Guido Fratesi,[b,e] Valeria Russo,[a] Andrea Li Bassi,[a] Sabine Maier[c] and Carlo S. Casari*[a]

Received 13th May 2025,
Accepted 19th November 2025

DOI: 10.1039/d5nr01968k

rsc.li/nanoscale

Graphdiynes are atomically thin carbon allotropes with mixed sp–sp^2 hybridization, able to self-assemble into diverse 2D and 1D nanostructures, from atomic layers to nanoribbons and molecular wires, with tunable optoelectronic properties beyond those of graphene. Here, we investigate novel graphdiyne molecular wires obtained *via* Ullmann coupling of 1,4-bis(bromoethynyl)benzene molecules on Au(100) and Au(111) surfaces. Using scanning tunneling microscopy (STM) and low-energy electron diffraction (LEED), we track the structural evolution of these systems under increasing annealing temperatures. Exploiting Raman spectroscopy, we perform the first-ever *in situ* monitoring of the thermally activated transition from organometallic to covalent organic wires (OMW-to-COW), resulting in the assignment of specific Raman features to both phases supported, by density functional theory calculations. We demonstrate that surface orientation affects the Ullmann coupling efficiency, resulting in a lower OMW-to-COW transition temperature on Au(100) than on Au(111). These findings provide new insights into the temperature-dependent structural dynamics of graphdiyne molecular wires, enabling the development of more efficient on-surface synthesis processes and the design of novel functional carbon nanostructures for new-generation optoelectronic devices.

Introduction

The recent discovery of atomically-thin carbon allotropes beyond graphene, *i.e.*, graphynes (GYs) and graphdiynes (GDYs), aroused huge interest within the scientific community.[1] These systems are characterized by a mixed sp–sp^2 carbon hybridization, and can rearrange into different 2D and 1D nanostructures with tunable sp/sp^2 ratio and porosity.[2–13] Thanks to the presence of diacetylenic linkages connecting benzene rings, GDYs overcome the zero-gap limitation of graphene, paving the way for new-generation semiconductor devices.[14,15] Moreover, the tunability of GDYs bandgap by means of doping, strain engineering or morphology modification, makes them highly appealing materials for optoelectronics and energy applications.[16–21] The interest in investigating 1D graphdiyne molecular wires (GDY MWs) arises from the outstanding predicted electronic, thermal and mechanical properties of carbyne, the ideal 1D carbon allotrope, consisting of an infinite chain of sp-hybridised carbon atoms. Its experimental realization has been considered elusive for a long time, due to the limited achievable extension of pure sp-carbon atomic wires.[22,23] To overcome this limitation, a possibility is to employ short carbon atomic wires as building blocks to form long sp–sp^2 carbon wires in which sp-carbon links bridge benzene rings.[24] Theoretical calculations predict intriguing properties for such sp–sp^2 atomic polymers, such as tunable band gap, very high electron mobility and size- and termination-dependent electronic transport.[25–28] Among recently developed bottom-up approaches for the synthesis of low-dimensional carbon nanostructures, on-surface synthesis (OSS) enables the formation of GDYs starting from (Br-functionalized) alkynyl precursors evaporated onto a noble metal surface acting as the reaction catalyst.[29–38] Evaporation of the precursor is followed by halogen cleavage from its alkynyl terminals, and the resulting carbon dangling bonds can undergo either a direct homocoupling reaction, generating CC covalent bonds, or coupling through metal adatoms from the underlying surface. In the latter case, the obtained inter-

---

[a] Department of Energy, Politecnico di Milano, via Lambruschini 6, 20156 Milano, Italy. E-mail: carlo.casari@polimi.it

[b] Department of Physics 'Aldo Pontremoli', Università degli Studi di Milano, Via G. Celoria 16, European Theoretical Spectroscopy Facility "ETSF", I-20133 Milano, Italy. E-mail: simona.achilli@unimi.it

[c] Department of Physics, Friedrich-Alexander Universität Erlangen-Nürnberg, Erwin-Rommel-Strasse 1, Erlangen, 91058, Germany

[d] Department of Chemistry, Università di Pavia, Via Taramelli 12, I-27100 Pavia, Italy

[e] INFN, Sezione di Milano, Milano, I-20133 Italy

mediate organometallic framework, under proper annealing conditions, can release the metal adatoms, allowing for the homocoupling to occur, resulting in the so-called organometallic-to-covalent transition.[30] The formation of ordered GDYs is very challenging, mainly due to the strong molecule–(metal)adatoms interaction and the reactivity of the sp-carbon phase, which tends to easily undergo crosslinking reactions and oxidation.[3,12,13,27,39–46] Moreover, strict control of the annealing temperature is needed to limit side reactions and desorption of the molecules from the substrate. The development of OSS processes under ultra-high vacuum (UHV) conditions allowed the formation of these novel carbon allotropes, and paved the way for their *in situ* scanning-probe microscopy/spectroscopy (STM/STS) investigations at the molecular level, unveiling GDYs structural, electronic and vibrational properties.[27,42]

Herein, we report on the surface- and temperature-dependent evolution of the atomic-scale structure and vibrational properties of graphdiyne molecular wires, monitored *via* STM and Raman spectroscopy, respectively. Recently, also X-ray photoelectron spectroscopy (XPS) proved to be a useful technique to monitor the Ullmann coupling process.[47] Despite the high sensitivity of XPS to oxidation states and elemental composition, Raman spectroscopy is extremely sensitive to carbon hybridization states,[48] making it particularly suited for studying GDY-like systems with a more accessible setup.

GDY MWs were obtained *via* on-surface synthesis under UHV conditions, starting from the evaporation of 1,4-bis(bromoethynyl)benzene molecules on Au(100) and Au(111). High-resolution STM imaging showed the transition from densely packed and highly oriented organometallic wires (OMWs) at room temperature, to progressively more disordered covalent organic wires (COWs) at higher temperatures, demonstrating that the activation temperature for the transition is lower on Au(100) than on Au(111). The higher efficiency of the OMW-to-COW transition on Au(100) than on Au(111) was also confirmed by Raman spectroscopy, which, supported by density functional theory (DFT) calculations, allowed us to assign for the first time peculiar vibrational features to the organometallic and covalent phases of the deposited systems. The combination of STM imaging and *in situ* Raman spectroscopy under UHV conditions allowed us to efficiently perform complementary analysis of the morphological and vibrational properties of these systems at the atomic scale, providing useful insights into the complex OSS process of sp–sp^2 carbon nanostructures, from molecular wires to extended frameworks.

Methods

Experiment

In situ experiments were carried out under UHV conditions, with a base pressure below 10^{-10} mbar. The employed system consists of two interconnected chambers, one for the preparation of samples and one for their characterization. Au(100) and Au(111) single crystal surfaces and Au(111) surface epitaxially grown on mica (MaTeck GmbH), were used as substrates for the OSS process. They were prepared through several cleaning cycles consisting of Ar^+ sputtering and annealing at 720–750 K, until STM inspection revealed wide terraces and negligible traces of organic contaminants. The molecular carbon precursor, *i.e.*, 1,4-bis(bromoethynyl)benzene (1,4-bBEB)[49] was loaded in powder form in a quartz crucible, which was then placed inside an organic molecular evaporator (OME) (MBE-Komponenten and Kentax). Being the precursor sublimation temperature in vacuum below room temperature (RT), the crucible was kept at 293 K through a water cooling system. However, due to its extremely high volatility even at such temperatures, to avoid the chaotic deposition of large amounts of disorganized molecules onto the metallic substrate, this one was kept far from the aperture of the OME, at an angle that hindered them from facing each other, and a very short deposition time was chosen as the optimal one. Specifically, the OME shutter was opened for 1 second, reaching a chamber pressure of 4×10^{-9} mbar. The substrate coverage was estimated by measuring the projected area occupied by the deposited molecules and is expressed in fractions of monolayer (ML), where 1 ML corresponds to 100% projected area. The as-deposited OMWs were characterized *via in situ* STM, LEED and Raman spectroscopy, then they were annealed for 15 minutes at progressively higher temperatures to follow the evolution of their morphological and vibrational properties during the OMW-to-COW transition. On Au(111), the explored range of temperatures was from RT up to 573 K, with intervals of 100 K. On Au(100), the explored annealing temperatures were from RT up to 353 K, with intervals of 20 K, then from 353 K to 383 K with intervals of 10 K and finally 473 K. Upon each annealing step, the sample cooled down to RT, and then STM and *in situ* Raman were exploited for a punctual monitoring of their atomic-scale structure and vibrational features.

STM measurements were carried out with two Omicron microscopes, one operating at room temperature (RT) and the other at 4.8 K (LT), using a home-made electrochemically etched tungsten tip and a Pt/Ir tip, respectively,[50] and the images were analyzed using the software Gwyddion.[51] Simulations of LEED patterns were obtained using the LEEDPat software (version 4.2), developed by K. Hermann and M. A. Van Hove. Raman spectroscopy was performed *in situ* with a portable InVia Renishaw spectrometer, having a spectral resolution of about 7 cm^{-1}. A 20× objective focused a green laser with 532 nm excitation wavelength on the sample through a non-absorbing viewport. The laser power delivered to the sample in UHV was approximately 36.5 mW, and several hundred spectral acquisitions were added up to obtain a satisfactory signal-to-noise ratio. Raman peaks were fitted through the software Fityk[52] using Voigt functions, after a careful background subtraction performed using Windows®-based Raman Environment (WiRE) software.

Theory

The *ab initio* calculations were carried out in the framework of density functional theory (DFT), exploiting GGA-functional[53] and a pseudopotential description of core electrons. A DFT approach with localized atomic orbital basis set, as implemented in the SIESTA code,[54] was adopted to study the structural and electronic properties of the system. For the calculation of phonons we adopted the density functional perturbation theory (DFPT),[55] based on plane wave description, as implemented in the QUANTUM ESPRESSO package.[56,57] Structural relaxations were performed by considering three layers of substrate, keeping fixed the two deeper layers and leaving free to relax the external surface layer and the adsorbed carbon network. We included van der Waals interactions between the organic overlayer and the substrate *via* a DFT-D2 Grimme potential.[58] The tolerance on forces was set to 0.04 eV Å^{-1}, the mesh cutoff for the real space grid was chosen equal to 400 Ry, and the supercell Brillouin zone was sampled with 120 *k*-points in all the considered adsorbed systems. In the case of isolated wires, 12 *k*-points were used to sample the Brillouin zone in the direction of the molecule. For the calculation of the electronic properties, the number of layers of the substrate was increased to six, and a five times denser *k*-grid was used to calculate the DOS. STM simulations were performed using the Tersoff–Hamann approach.[59] Phonon calculations at the Γ-point were performed after a refinement of the structural relaxation using plane-waves, ultrasoft pseudopotentials from PSlibrary,[60] 50 Ry and 400 Ry as cutoff for the wavefunction and charge density, and the same *k*-points as in SIESTA calculation.

Results and discussion

On-surface synthesis *via* Ullmann coupling under UHV conditions was exploited to obtain graphdiyne molecular wires, starting from the evaporation of 1,4-bBEB molecules (Fig. 1a) onto different gold surfaces, namely Au(100) and Au(111), kept at room temperature (RT). The process consists of three basic steps, depicted in Fig. 1b: diffusion of the molecules along the metal surface, cleavage of the C–Br bond with subsequent chemisorption of the molecules on the metal surface through metal adatoms, resulting in stable OMWs, and, finally, thermally-activated removal of the metal adatoms followed by C–C homocoupling, leading to the formation of COWs.

Atomic-scale structure of GDY organometallic wires

Fig. 2 shows large-scale and atomically resolved STM images of as-deposited OMWs on Au(111) and Au(100) surfaces, obtained after 1-second exposure of the metallic substrate to the evaporated precursor. On both surfaces, OMWs form densely packed and highly oriented domains organized over the surface according to its symmetry.

On Au(111) (Fig. 2a), characterized by a hexagonal lattice of period 0.289 nm, the organometallic domains are aligned along six directions, grouped in three-by-three equivalent directions rotated by 60° from each other and labeled for clarity: a, b, c, a*, b*, c*, respectively. From the analysis of reciprocal space images (2D fast Fourier transform, or 2D FFT), it is possible to extract the domains' rotation angle with respect to the surface directions, as detailed in Fig. S1. Fig. 2a shows an example of sub-monolayer coverage: indeed, the packed OMW domains leave exposed a few regions of the gold surface, on which Br atoms accumulate forming a $(\sqrt{3} \times \sqrt{3})\text{R}30°$ overlayer,[61,62] as well as at the edges of the domains, upon molecules' dehalogenation. The Br reconstruction induces a partial distortion of the Au(111) herringbone reconstruction that, at this coverage, acts as a constraint for the OMWs, resulting in anisotropic domains, as can be observed in more detail in Fig. S2. The presence of Br atoms also underneath the organometallic network cannot be excluded, as previously observed on different carbon nanostructures.[63] However, the investigation of the role of Br atoms in the synthesis of these networks is out of the scope of the present work.

On Au(100) (Fig. 2b), characterized by a square lattice of period 0.289 nm, the domains are organized along four directions (cyan and green arrows), arranged in two perpendicular pairs, with each pair forming an angle of ≈30° and ≈60° with the [011] and $[01\bar{1}]$ directions of the Au(100) surface, as shown in the inset and in Fig. S3.[64,65]

OMWs are arranged over both Au(111) and Au(100) surfaces according to two configurations, a close-packed and a noncompact one. In the most common configuration, the organometallic wires are arranged over Au(111) and Au(100) in highly

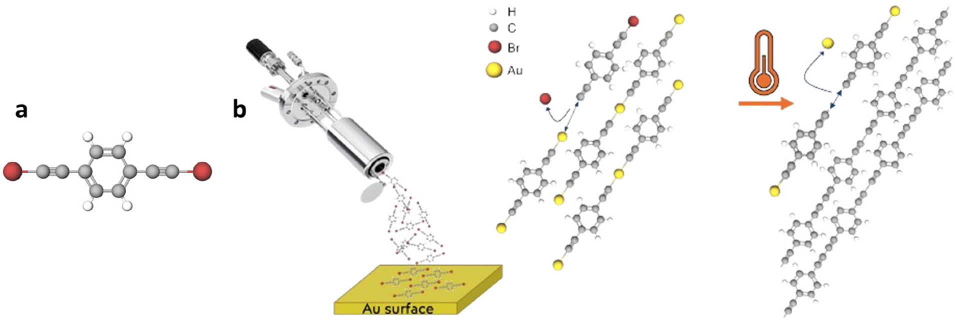

Fig. 1 (a) Ball-and-stick atomic model of the 1,4-bi(bromoethynyl)benzene (1,4-bBEB) molecular precursor. (b) On-surface synthesis of 1,4-bBEB-based GDY MWs on gold surfaces.

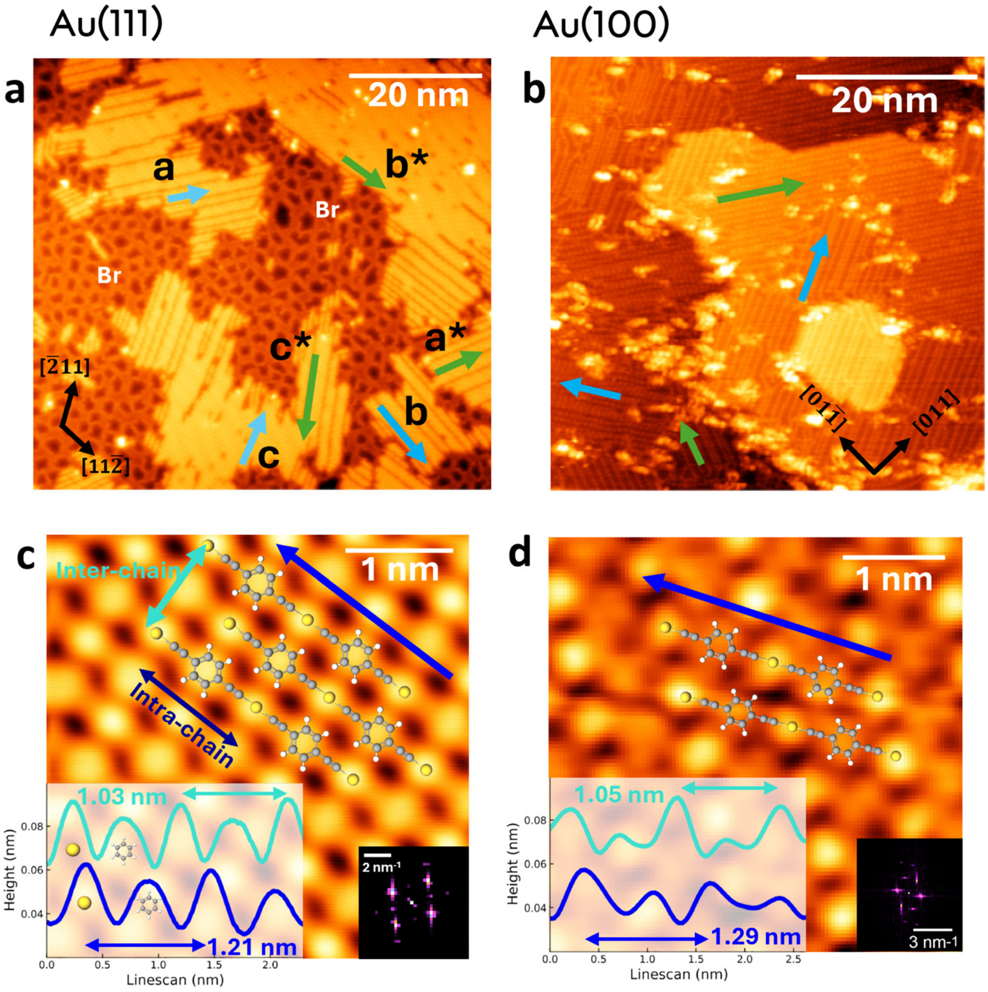

Fig. 2 Large-scale LT-STM (a) and RT-STM (b) images of the as-deposited OMWs on Au(111) and Au(100), respectively, after 1 s of exposure to the molecular beam. The cyan and green arrows in (a) and (b) indicate the orientation of the OMW domains. The black arrows in (a) and (b) indicate the high symmetry directions of Au(111) and Au(100), respectively. Br atoms are the fainter dots labeled in white colour in (a), forming a porous network. Bottom panels show atomically resolved LT-STM (c) and RT-STM (d) images of a densely packed domain of OMWs on Au(111) and Au(100), respectively. Left bottom insets in (c and d): height profiles measured along the chain direction (blue) and perpendicularly to it (cyan), with the corresponding averaged intra- and inter-chain periodicity values. Brighter spots correspond to Au adatoms, fainter spots to benzene rings – see superimposed ball-and-stick atomic model. Right bottom insets in (c and d): 2D-FFT showing the reciprocal cell of the close-packed OMWs domains on Au(111) and Au(100), respectively. STM set-points: (a) 1 V, 10 pA, (b) 0.70 V, 0.40 nA, (c) 3 mV, 0.12 nA, (d) 0.70 V, 0.20 nA.

compact domains, showing a perfect alternation of gold adatoms and benzene rings in both the wires' direction and perpendicularly to it (see Fig. 2c and d). The high compactness of these domains does not allow for the hosting of Br atoms in between the wires. In the less common configuration, the organometallic wires are arranged over the gold surface in less compact domains, where the alternation of gold and benzene rings in the direction perpendicular to the chains is lost, leading to a larger spacing between the chains (see Fig. S4) that allows for the hosting of Br atoms, as it was already observed in previous works.[27] Fig. 2c and d shows atomically-resolved images of as-deposited OMWs on Au(111) (c) and Au (100) (d), exhibiting the characteristic alternation of bright and faint spots, corresponding respectively to the bridging Au adatoms and benzene rings.[3,27] This is also confirmed by the height modulation observable in the topographic profile (bottom inset of Fig. 2c and d).

The lattice periodicity of the OMW domains, along both the wires direction (intra-chain periodicity) and perpendicularly to it (inter-chain periodicity) was extracted from topographic profilometry measurements performed on several close-packed OMW domains found in different regions of the Au(111) and Au(100) surfaces. In particular, topographic profiles were acquired over several high-resolution STM images at different bias, and the periodicity values were extracted by averaging over different lines along the intra-chain and the inter-chain directions, respectively. On Au(111), the high-resolution LT-STM images of the $(\sqrt{3} \times \sqrt{3})R30°$ overlayer formed by Br atoms were used to extract a calibration factor that allowed for determining the accurate periodicity values for the OMWs (see

Fig. S5). These values were further averaged over several different images. The close-packed OMW domains deposited on Au(111) show an intra-chain periodicity of 1.21 ± 0.02 nm and an inter-chain periodicity of 1.03 ± 0.02 nm. On Au(100), the averaged intra-chain periodicity for the close-packed OMW domains is 1.29 ± 0.03 nm, while the inter-chain one is 1.05 ± 0.05 nm. By comparing Fig. 2d with Fig. S4, it is possible to observe the abovementioned increase in the interchain periodicity, from 1.05 nm to 1.28 nm, going from the close-packed to the non-compact OMWs configuration, which allows for the hosting of Br atoms in between the chains. 2D FFT of the STM images of the two systems (Fig. 2c and d) gives an oblique reciprocal cell for both the OMW domains obtained on Au(111) and Au(100), with lattice vectors forming an angle of 97° ± 1° and 94° ± 2°, respectively.

To confirm the obtained intra-chain periodicity value for the close-packed OMW domains, LEED experiments were conducted on Au(100) single crystal surface, before and after their deposition. In Fig. S6a, both the first-order LEED pattern of Au (100) lattice and the surface reconstruction along [011] and [01$\bar{1}$] are shown, being the latter recognizable through the typical split diffraction spots.[66] The LEED pattern of the OMW domains deposited on Au(100) surface is shown in Fig. 3. The sub-monolayer coverage makes it possible to observe the first-order spots of both Au(100) surface reconstruction and the OMW domains, with spots describing 2 pairs of perpendicular directions, each rotated by 30° and 60° with respect to Au [011] and [01$\bar{1}$] directions.

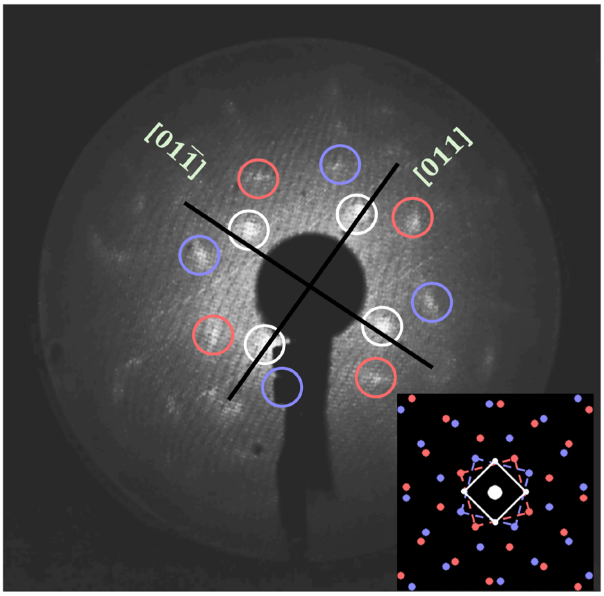

Fig. 3 First order LEED diffraction pattern at 20 eV of the OMW domains deposited on Au(100). The black lines indicate the crystallographic directions of the Au(100) surface. Circled spots: white indicates the first order spots of the Au(100) surface reconstruction, pink and violet indicate the first order spots of the OMW domains, paired two by two in perpendicular directions. Inset: simulated LEED pattern through the superlattice matrix $\begin{pmatrix} +3.88 & +2.24 \\ -2.24 & +3.88 \end{pmatrix}$. The first order spots of the Au(100) surface reconstruction have been added manually to the simulated pattern.

From the LEED analysis, it is possible to extract an intra-chain periodicity of 1.28 ± 0.03 nm, which matches the experimental one obtained by STM images analysis. This interpretation is further corroborated by the correspondence between the experimental LEED pattern (Fig. 3) and the simulated one for the analyzed system (inset of Fig. 3), obtained by considering an incommensurate square superlattice having an intra-chain periodicity equal to 1.29 nm and an angle of 30° (60°) with respect to gold [011] ([01$\bar{1}$]) direction, as extracted from STM measurements.

Theoretical structural model of GDY OMWs on Au surfaces

Based on the information extracted from STM and LEED measurements, we built a suitable model for the structure of packed OMWs on Au(100) and Au(111), reported in Fig. 4a and b. The theoretical intra-chain periodicity of the freestanding organometallic and covalent organic wires is 1.21 nm and 0.95 nm, respectively, while the equilibrium inter-chain distance amounts to 0.95 nm. These values are compatible with the periodicity of Au(100) and Au(111) surfaces along specific directions, allowing the formation of superstructures with a reasonable percentage of strain.

Although the matching is forced by the computational requirement of in-plane periodic boundary conditions, the commensurability introduced in the calculation is expected not to alter the properties of the system in virtue of the quite small strain applied to the molecules. Moreover, the simulation cells include more than one molecular unit in the wire, displaying a different stacking with respect to the underlying substrate, so that the local interaction with the metal is not forced to be the same for all the wires but different types of local arrangements are included in the model.

For the OMW domains grown on Au(111), we adopt a supercell with epitaxial matrix $\begin{bmatrix} 2 & 5 \\ 4 & 1 \end{bmatrix}$ with respect to the Au(111) lattice vectors in the [$\bar{1}$10] and [10$\bar{1}$] directions. The OMWs form an angle of 6.6° with the [1$\bar{1}$2] direction, in good agreement with the experiments. The intra-chain periodicity in the model is 1.29 nm, while the inter-chain distance is 1.07 nm. The angle formed by the two vectors of the unit cell is 97°, in agreement with the experimental estimate. The strain imposed on the OMWs to fit the crystal supercell amounts to 6.6% with respect to the theoretical freestanding polymer. We obtain a calculated binding energy equal to 4.31 eV per molecule. For the same system, we also considered other possible structural models to disentangle, in the binding energy, the effect of the strain and the contribution given by the interaction with the substrate. They are reported in Fig. S7.

The constant height (d = 0.2 nm) STM simulation (Fig. 4c) obtained by integrating the empty states in the energy range [E_F, 0.5 eV], shows the alternation of brighter spots, corresponding to Au adatoms, and fainter spots, due to the benzene rings, confirming the experimental assignment.

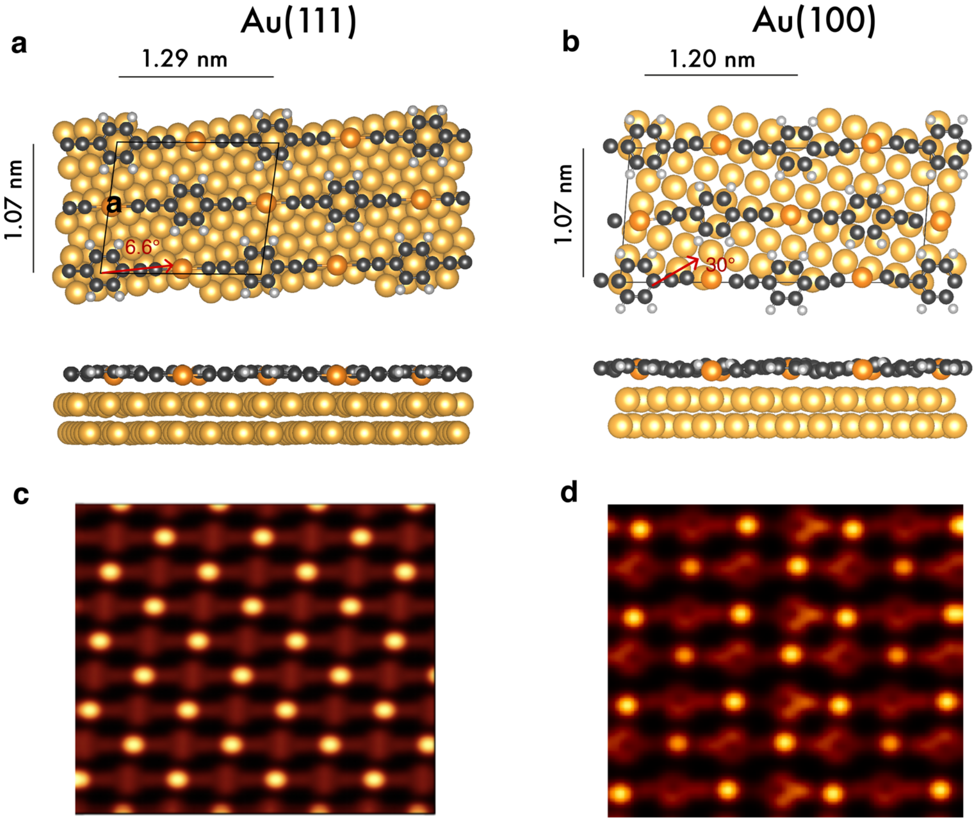

Fig. 4 Structural model adopted in the calculations for OMW domains on Au(111) (a) and Au(100) (b) and associated STM simulation: OMW on Au (111) (c), and OMW on Au(100) (d), at a bias of +0.5 eV. Red arrows in (a) and (b) mark the [1$\bar{1}$2] and [011] directions, respectively, and the angle described by OMW reported accordingly.

On the basis of experimental findings, for the OMW domains grown on Au(100) we adopted a supercell with epitaxial matrix $\begin{bmatrix} 7 & 4 \\ 2 & -3 \end{bmatrix}$ with respect to the lattice vectors in the [011] and [01$\bar{1}$] directions. This supercell, containing four molecular units (Fig. 4b), enables the matching with the substrate with an intra-chain periodicity of 1.20 nm and a negligible compressive strain of 0.8%. In the direction perpendicular to the OMWs, the separation between parallel wires is 1.07 nm, slightly larger than in the experiment but in agreement with the periodicity adopted for Au(111), which turns to be more stable than other possible choices. The angle between the two vectors defining the supercell is equal to 94°, fully overlapping with the one extracted from the experimental 2D-FFT, while the one between the OMWs and the [011] direction is 30°, reproducing the experimental observation.

The adsorption energy of the OMW domains on Au(100) is equal to 5.30 eV per molecule, slightly larger than the one calculated for Au(111) in the model reported above. This is related to the smaller strain introduced in the molecular wire on Au(100) (for a discussion of this effect, see also Fig. S8).

Also on Au(100), the constant-height simulated STM image confirms the assignment of bright spots to gold atoms and fainter features to benzene rings.

Upon relaxation, on both the surfaces, molecules are mildly distorted in plane and slightly buckled out of plane. As a consequence of Au–Au interaction, the adsorption distance of Au adatoms is smaller than the one of benzene rings, leading to a tiny bending of the structure. The average equilibrium adsorption distance is 0.27 nm on Au(111) and 0.26 nm on Au(100), while the buckling of the overlayer is lower than 0.1 nm.

The calculated electronic properties of the OMWs on Au (100) and Au(111) are quite similar. Both surfaces show an electronic charge transfer from the gold to the OMWs (0.27 e per molecule for Au(100) and 0.20 e per molecule for Au(111)). This is due to an increase in the electronic charge on carbon and hydrogen atoms and a depletion of Au adatoms, being such depletion slightly more pronounced on Au(111) than on Au(100) (0.15 e per molecule *versus* 0.13 e per molecule).

Surface-dependent thermal efficiency of the organometallic-to-covalent transition

To study the evolution of the wires with temperature, we progressively increased the annealing temperature to the as-deposited organometallic system (see Methods section for the detailed steps) and performed STM imaging upon each annealing treatment.

In Fig. 5, the thermally-dependent evolution of the atomic structure of the MWs domains on Au(111) and Au(100) is

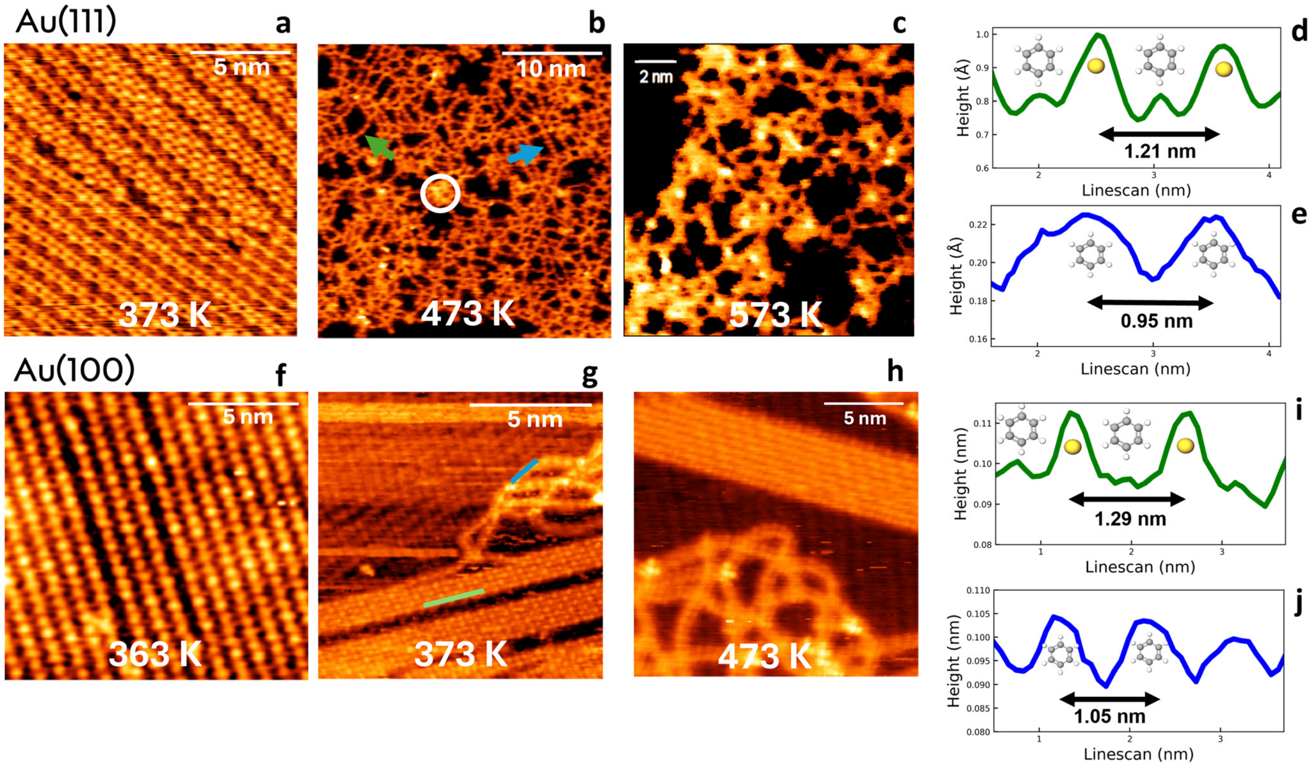

Fig. 5 (a–c and f–h) Atomically-resolved STM images of the MWs domains grown on Au(111) and Au(100) upon different annealing conditions. (d–e) Height profile measured along the organometallic and covalent organic wire, indicated by the green and blue arrows in (b), respectively. (i and j) Height profile measured along the organometallic and covalent wire indicated by the green and blue lines in (g), respectively. STM set-points: (a) 0.25 V, 0.20 nA (b) 0.30 V, 0.25 nA (c) 0.30 V, 0.25 nA, (f) 0.30 V, 0.25 nA, (g) 0.30 V, 0.25 nA, (h) 0.30 V, 0.25 nA.

shown. On Au(111) (Fig. 5a–e), upon mild annealing at 373 K, the system is still highly ordered and completely organometallic, with an averaged intra-chain periodicity of 1.21 nm ± 0.03 nm, corresponding to the one obtained just after the evaporation, already observed in Fig. 2c. An increase in the annealing temperature to 473 K leads to the partial release of gold adatoms from the domains, together with their partial homocoupling. In fact, by looking at the height profiles reported in Fig. 5d and e, it can be deduced that, at 473 K, both the organometallic and covalent phases are present, with an intra-chain periodicity of 1.21 nm and 0.95 nm, respectively, being the latter in agreement with the value predicted by our DFT calculations. It is worth mentioning that if, on one side, the release of the gold adatoms results in the CC homocoupling between adjacent de-metalated wires, on the other side, it also causes the distortion and consequent relaxation of the wires into a partially disordered system. Moreover, cross-linking side reactions within the OMWs can lead to the formation of amorphous regions, exemplified by the white-circled region of Fig. 5b. At 573 K, gold adatoms are mostly removed, and the system undergoes the complete loss of long-range order, showing an averaged intra-chain periodicity of 0.95 nm, corresponding to the one of the covalent organic phase. Br atoms are expected to desorb from gold at a temperature of approximately 520 K;[67] therefore, we can assume that, upon annealing at 573 K, most of them have been removed from the surface, favouring the de-metalation of the residual organometallic wires and the obtainment of a mostly covalent system. On the other side, a role of Br atoms desorption in the progressive increase of the disorder of the system cannot be excluded. Despite the highly local nature of STM, the averaged periodicity extracted from a series of different high-resolution images of different regions of the sample, combined with the macroscopic information extracted from the Raman investigation of the system (see next subsection), allowed us to extend its local behaviour to the whole sample.

The same general behaviour was found for the systems deposited on Au(100) (Fig. 5f–j). Upon mild annealing at 363 K, the system is highly ordered, with an average intra-chain periodicity matching the one of the as-deposited OMW domains, *i.e.*, 1.29 nm. Remarkably, the removal of gold adatoms starts at about 373 K, a lower temperature than the one needed by the system grown on Au(111), which was about 473 K. In fact, by looking at the height profiles reported in Fig. 5i–j, it can be deduced that both the organometallic and covalent phases are already present at 373 K, with an intra-chain periodicity of 1.29 nm and 1.05 nm, respectively. In particular, the still well-ordered islands correspond to the organometallic phase, as can be better appreciated by the line profile in Fig. S9, while the disordered regions correspond to the covalent phase. At 473 K, the disordered covalent phase is the dominant one, even though the ordered organometallic phase is still present, but with a lower extent with respect to Au(111). This surface-dependent behaviour can be understood based on a different interaction between the Au adatoms and the surface, possibly mediated also by the presence of Br adatoms on the surface that help maintain the linear ordering of the wires.

To investigate the strength of the interaction between the Au adatoms and the two surfaces, we performed electronic calculations mimicking the de-metalation process. We considered a very large supercell, with two adsorbed 1,4-bBEB molecules connected *via* a gold adatom and terminated by Br, to be representative of the smallest possible unit occurring in the demetalation process (Fig. S10). The choice of a finite molecule instead of the polymeric counterpart allows for reducing the number of atoms in the simulation and avoiding polymerization-related effects. In this sense, the termination with Br atoms seems to be the most natural choice, since the adopted system is representative of a single de-metalation process in two joined molecules that preserve their pristine ending Br atoms. The COW unit is instead represented by the system in which the Au adatom has been removed.

We calculated the energy required to remove the Au atom from the molecule, considering, as final state, a configuration in which the Au is an adatom on the surface, far from the molecule, and the dimer has been recomposed by shifting one half of the molecule to attach to the remaining part. The same procedure was performed on Au(100) and Au(111), by taking supercells of similar size to treat the interaction between periodic replicas of the molecule on the same footing. Although the energy difference between the initial and final configurations is not the energy barrier necessary to remove the adatom, it provides a useful estimate of the energy cost of the process. Such energy cost was calculated to be equal to 0.28 eV on Au(111) considering the Au atom in the dimer lying in hollow position with respect to the surface. This barrier reduces to 0.15 eV and 0.20 eV on Au(100), for the adatom in hollow position and on top of an atom in the second layer of the surface, respectively. In both cases, the energy cost to extract the adatom is lower on Au(100) than on Au(111), *i.e.*, 0.13 eV and 0.08 eV, respectively. Although an adatom on the bare surface would indeed be more strongly bound on Au(100) than on Au(111), in virtue of a larger local coordination, here the larger energy required to remove the adatom from the molecule on Au(111) is due to the additional contribution of the intramolecular interaction between Au and nearby carbon atoms. Moreover, the lower binding energy on Au(100) can also be due to the different stability of the covalent organic molecule on the two surfaces in virtue of their different stacking with respect to the surface.

Insight on temperature-dependent vibrational properties

We performed *in situ* Raman spectroscopy under UHV conditions to follow the OMW-to-COW transition, since this technique provides insight into the local bond information, especially related to sp- and sp^2-carbon hybridization. Through this technique, we could assign specific Raman features to the organometallic and covalent phases of the deposited wires for the first time. Moreover, we confirmed the STM-based evidence of the structural changes occurring within the MWs domains during the thermally-activated OMW-to-COW transition, together with its surface-dependent efficiency. Fig. 6a shows, in green, the experimental Raman spectrum of the 1,4-bBEB powdered precursor. Based on the phonon calculation reported below, B′ (1182 cm^{-1}) and B″ (1236 cm^{-1}) correspond to in-plane and out-of-plane bending of the C–H bonds, sp^2 (1604 cm^{-1}) corresponds to C═C breathing of benzene, Y (2194 cm^{-1}) and Y′ (2217 cm^{-1}) are respectively the in-phase and out-of-phase stretching of the –C≡C– bonds, being indeed in the spectral region characteristic of the Effective Conjugation Coordinate (ECC) mode, *i.e.*, the collective sp-carbon stretching mode (expected between 1800 and 2300 cm^{-1}). According to the theoretical calculation of phonon modes for the isolated 1,4-bBEB molecule, the C–Br stretching modes fall in the 500 cm^{-1} region. This can be appreciated in Fig. S11, where the *ex situ* Raman spectrum of the 1,4-bBEB molecules in powder form and the *in situ* Raman spectrum of the as-deposited OMW on gold are compared. In particular, the two peaks at 463 cm^{-1} and 523 cm^{-1} observable in the *ex situ* Raman spectrum of the powder precursor and associated to the C–Br stretching modes, disappear upon molecules evaporation on gold, confirming the successful dehalogenation process. The incorporation of the Au adatom in the polymerization process induces non-negligible effects on the vibrational properties of the precursor,[39] as can be observed by comparing its Raman spectrum with the one of the as-deposited OMWs on Au(100), in black (Fig. 6a). The most prominent variation is the broadening and downshift to 2023 cm^{-1} of the ECC mode due to C–Au coupling through the metal adatoms, which determines the weakening of the stretching force constants of the –C≡C– bond. To distinguish the sp-carbon stretching mode in the precursor from the one in the OMW, the latter will be denoted as sp_{OMW} from now on. Other differences between the precursor and the OMW spectra are the quenching of B″ mode, likely due to the surface-induced planarity of the deposited OMW domains, and the broadening and structuring of the sp^2 peak. Fig. 6b and c show the experimental Raman spectra acquired for the deposited wires on Au(100) at RT and upon annealing at progressively higher temperatures, ranging from 313 K to 473 K. We focused on the sp- and sp^2-carbon spectral regions, being the ones that allow us to monitor punctually the OMW-to-COW transition. The sp_{OMW} peak shows a progressive intensity decrease as a function of increasing temperature (Fig. 6b) from RT to 473 K. On the other side, starting from 313 K, a new peak appears at 2178 cm^{-1}, whose intensity increases with temperature, until it becomes the dominant one at 473 K. The opposite trend of these two peaks, combined with the information extracted from the STM analysis as a function of the temperature, reported in previous sections, suggests that the two peaks can be considered as the fingerprint of the OMW-to-COW transition. According to this interpretation, the decrease in sp_{OMW} peak intensity corresponds to the progressive removal of gold

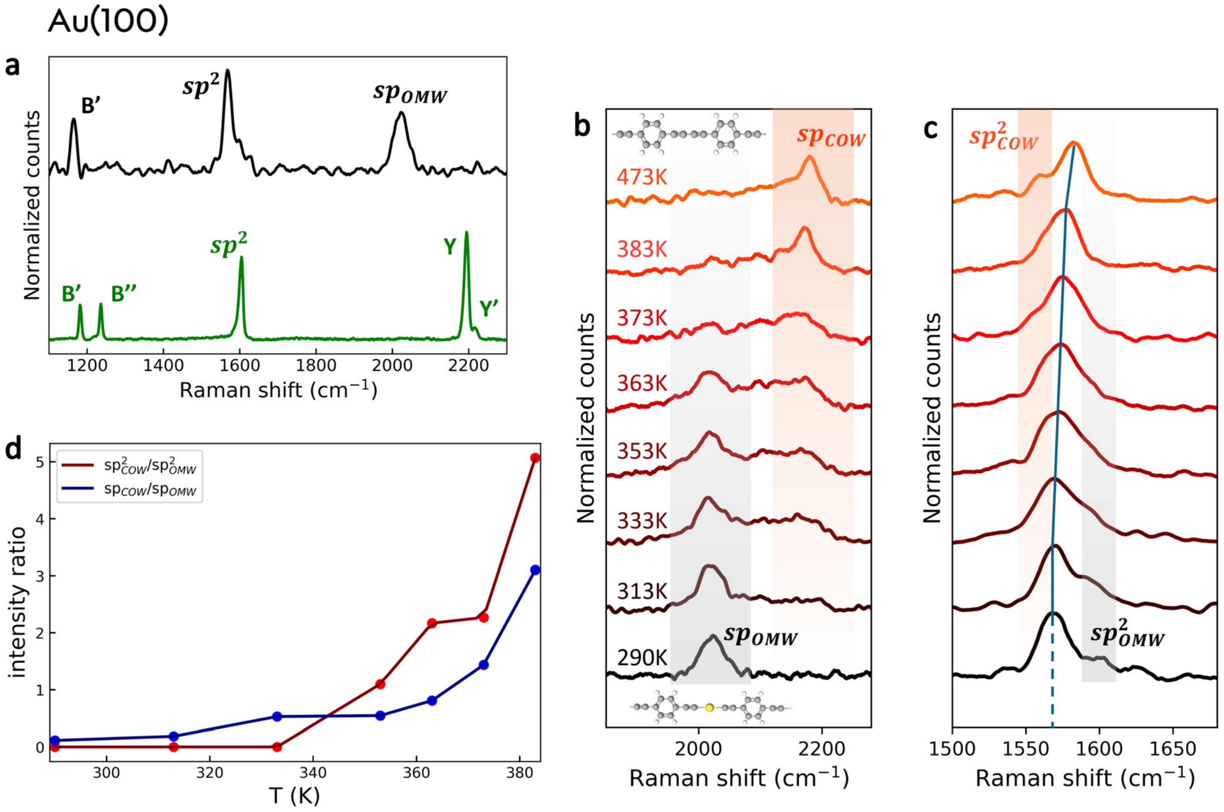

Fig. 6 (a) Normalized Raman spectra of 1,4-bBEB precursor (*ex situ*, green) and corresponding as-deposited OMWs on Au(100) (*in situ*, black). Laser parameters: 532 nm excitation wavelength, 0.7 mW (*ex situ*), 36.5 mW (*in situ*) power delivered to the sample. (b) Normalized Raman spectra of the MWs grown on Au(100) (sp-carbon region) as a function of the applied annealing temperature. The ball-and-stick atomic models of the organometallic wire (bottom) and covalent organic wire (top) are reported for clarity. (c) Normalized Raman spectra of the MWs grown on Au(100) (sp^2-carbon region) as a function of the applied annealing temperature. The dark blue line indicates the blueshift of the main sp^2 peak component. (d) sp$_{COW}$/sp$_{OMW}$ (blue) and sp$^2_{COW}$/sp$^2_{OMW}$ (red) intensity ratio for the MWs grown on Au(100) as a function of the applied annealing temperature.

adatoms from the OMWs, and the simultaneous specular increase in the newly appeared sp-carbon peak intensity corresponds to the progressive homocoupling of the system. For this reason, the peak at 2178 cm^{-1} will be from now on labelled as sp$_{COW}$. Despite the transition from organometallic to covalent phase is not complete over the whole sample, the progressive increase in the intensity of the sp$_{COW}$ peak with respect to the sp$_{OMW}$ peak as a function of the applied annealing temperature can be well appreciated in Fig. 6d (blue curve). It is also possible to observe a slight broadening in the sp$_{COW}$ peak from 383 K to 473 K, that could be due to the progressive thermally-activated increase in the degree of disorder of the COWs, which could bring to their partial cross-linking.

To support the assignment of the Raman peaks in the sp-carbon spectral region and to confirm the relationship between their evolution and the OMW-to-COW transition, we performed *ab initio* calculations of the phonon modes of both the freestanding OMW and COW domains at zone center (q = 0), and we compared them with those of the isolated 1,4-bBEB molecule (Fig. 7).

The calculated frequencies for the –C≡C– stretching mode in the isolated 1,4-bBEB molecule are 2219 cm^{-1} and 2226 cm^{-1} for the in-phase and out-of-phase vibrations (Fig. 7a and Fig. S15), respectively, in reasonably good agreement with experiments.

The corresponding modes, in the OMW, are redshifted to 2084 cm^{-1} and 2040 cm^{-1}, respectively, while, in the COW, they blueshift again to 2192 cm^{-1} and 2155 cm^{-1}, respectively (Fig. S15). These findings are in agreement with what was observed in the experiments, *i.e.*, the lowering of the phonon frequencies in the OMW domains and their upshift upon adatom removal (see Fig. 7a). Interestingly, this agreement is achieved by considering isolated carbon systems, *i.e.*, by neglecting the effect of the substrate. This suggests that the softening of the phonon modes in the OMW domains and their blueshift in the COW ones are essentially due to the intra-chain interaction between C and Au adatoms and, to a smaller extent, to the interaction between the MWs and the substrate.

To clarify the origin of the phonon modes softening, we performed calculations in which the mass of the terminal Br atoms was artificially increased in 1,4-Br-bBEB, resulting in the same frequencies for the calculated sp vibrational modes, meaning that the softening was not due to a "mass effect". Differently, by substituting Br atoms with Au atoms, we obtained a partial softening of the ECC mode (stretching modes at 2166 and 2178 cm^{-1}), as reported in Fig. S15c and d, confirming that the observed effect is

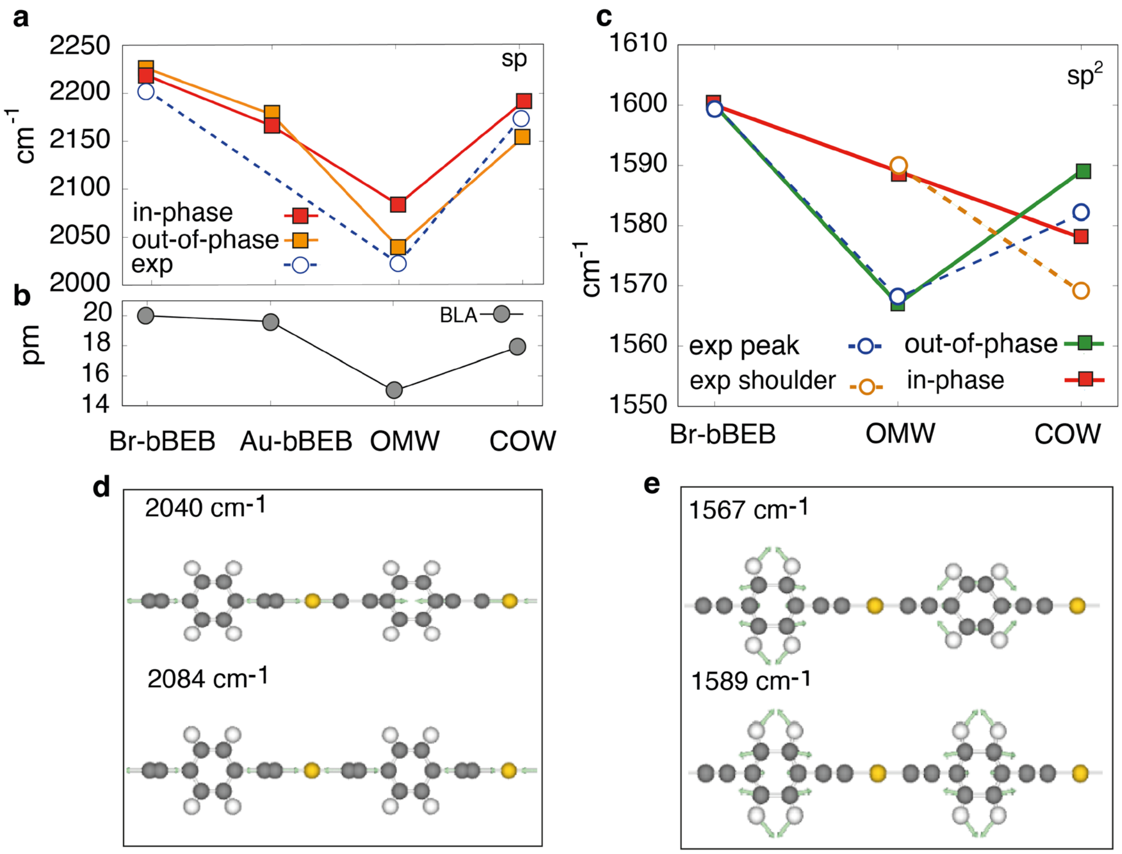

Fig. 7 Frequencies, calculated and measured (a) and bond length alternation (b) of −C≡C− stretching modes in freestanding OMWs. Red: in phase −C≡C− stretching mode, orange: out of phase −C≡C− stretching mode, blue: experimental fit of the Raman peak frequencies. (c) Calculated and measured frequencies of modes involving benzene rings. Red: in phase-benzene breathing mode, green: out of phase benzene breathing mode, blue: experimental fit of the main Raman peak, orange: experimental fit of the Raman shoulders nearby the main peak representing the softening of the "in phase" vibrational mode during the OMW-to-COW transition. (d and e) Atomic displacements of the symmetric "in phase" and antisymmetric "out of phase" phonon modes of OMWs (phonon modes of other species are reported in SI). Experimental data are extracted from Fig. 6.

due to a change of the force constant. The trend observed for the frequencies, both in the calculated phonons and in the Raman experiments, follows the same trend of the calculated bond length alternation (BLA) (Fig. 7b), which is smaller for the OMW and larger for the 1,4-bBEB molecule and the COW. Thus, we can conclude that the observed changes in the frequencies are a fingerprint of the variation of conjugation in the system. On the other hand, the frequency change could be related to the different number of sp-carbon units in the wire (one in OMWs, two in COWs). Although the wires are too short to allow a comparison with the trend observed for longer polymers[68] (that would be opposite, that is, softening observed for longer molecules), their behaviour agrees with the data available for short C_nH_2 chains.[69]

The same approach can be applied also to follow the evolution of the sp^2 peak as a function of the annealing temperature (Fig. 6c and Fig. S12). From RT up to 333 K, the sp^2 peak can be deconvoluted in two components, located at 1590 cm^{-1} and 1569 cm^{-1}, respectively (Fig. S12a–c). From 353 K up to 383 K, it is possible to observe a monotonic blueshift of the main peak, namely from 1569 cm^{-1} to 1579 cm^{-1}; moreover, the deconvolution results in the appearance of a third, new, component, located at 1561 cm^{-1} (Fig. S12d–f), whose intensity increases with the temperature. Finally, at 473 K, the main peak is further blueshifted to 1582 cm^{-1}, and the component at 1590 cm^{-1} disappears (Fig. S12g). The temperature dependence of the main sp^2 peak resembles the one presented above for the sp peak. Indeed, also in this case, it is subjected to a progressive blueshift (from 1569 cm^{-1} to 1582 cm^{-1}) as a function of the applied annealing conditions, following the OMW-to-COW transition. The other two sp^2 components at 1590 cm^{-1} and 1561 cm^{-1} coexist only in a limited annealing temperature range, from 353 K to 383 K (Fig. S12d–f), while they mutually exclude when the system is completely organometallic (*i.e.*, from RT up to mild annealing conditions) and mostly covalent (*i.e.*, at 473 K), as shown in Fig. S12a–c and S12g, respectively. This evidence suggests that the component located at 1590 cm^{-1} could be assigned to the organometallic phase (sp^2_{OMW} in Fig. 6c), while the component located at 1561 cm^{-1} to the covalent phase (sp^2_{COW} in Fig. 6c). This hypothesis is further corroborated by looking at the intensity ratio between the sp^2_{COW} and the sp^2_{OMW} components, plotted as a function of the annealing temperature (Fig. 6d, red curve). Its monotonic increase suggests that at 353 K the removal of gold adatoms from the OMWs begins, together with the homocoupling, but the majority of the system is still organometallic, while by increasing the temperature the amount of the covalent organic phase progressively overcomes the organometallic one, until becoming the dominant one at 373 K.

The same general trends in the temperature-dependent Raman responses of the MWs were observed on Au(111) (Fig. S13), therefore, their detailed discussion has been omitted. Also on Au(111), the range of explored annealing temperatures did not allow for the transformation of the entire sample from organometallic to covalent, even though, from Raman spectroscopy, it is evident that at 573 K the covalent phase is the dominant one.

From the reported Raman analysis, it is clear that the temperature at which the covalent phase becomes dominant is 573 K on Au(111) and 473 K on Au(100). The higher temperature required for the transition from OMW to COW on Au(111) leads, as a secondary effect, to a remarkable distortion of the network, compared to what is observed on Au(100). Indeed, by looking at the STM images in Fig. S14b, it is evident that, on Au(100), the covalent phase, coexisting at that temperature with the well-ordered organometallic phase, is less distorted than on Au(111) (Fig. S14a), on which the higher temperature required to generate the COW turns the system into a highly distorted and cross-linked covalent phase.

A remarkable difference in the set-point temperature for the OMW-to-COW transition on Au(111) with respect to Au(100) is demonstrated, as detailed in the following.

In Fig. 7c, we report the comparison between the experimental and calculated phonon frequencies for the breathing modes of benzene ring modes around 1600 cm^{-1}. The phonons have been calculated in a supercell containing two molecular units, to have access to both the symmetric mode, with benzene rings vibrating in phase, and the antisymmetric modes, with benzene rings vibrating out of phase. In the transition from organometallic wires to covalent organic wires, the symmetric mode and the antisymmetric mode (Fig. 7e and Fig. S15) behave differently. The "out-of-phase" mode displays an initial softening, passing from the 1,4-bBEB molecule to the isolated OMW, followed by an increase in frequencies upon transition from OMW to COW. This theoretically predicted behavior, similar to the one observed for the sp-carbon stretching mode, matches the evolution of the main experimental sp^2 peak, discussed above. Differently, the "in phase" vibration exhibits a continuous progressive softening, from the 1,4-bBEB molecule to the isolated OMW, and then to the COW. The same effect can be observed in the experimental data, considering the two shoulders on the right and left of the principal peak (Fig. 6c), resulting from the peak deconvolution discussed above and represented by the two orange dots in Fig. 7c. Based on the calculations (red line), they can be interpreted as the same peak, indeed ascribed to the "in phase" vibration mode, which becomes softer during the transition from organometallic to covalent organic wires (dashed line connecting the two dots).

Notably, the "out-of-phase" mode follows the same trend of the sp-carbon peak during the evolution of the system, meaning that it is affected by the strength of the carbon–carbon bonds in the chain, and, in particular, by the variation of the bond between the sp^2 terminal atom in the benzene moiety and the first sp-carbon atom in the chain. On the other hand, the "in phase" vibration can be hampered by the shortening of the chain upon the release of the adatoms, which leads to the reduction of the distance between benzene rings. Moreover, we found an involvement of the carbon atoms of the chain in the "in phase" vibration mode, which is instead negligible in the "out-of-phase" mode, and that could act as a counter-motion hindering the benzene breathing modes.

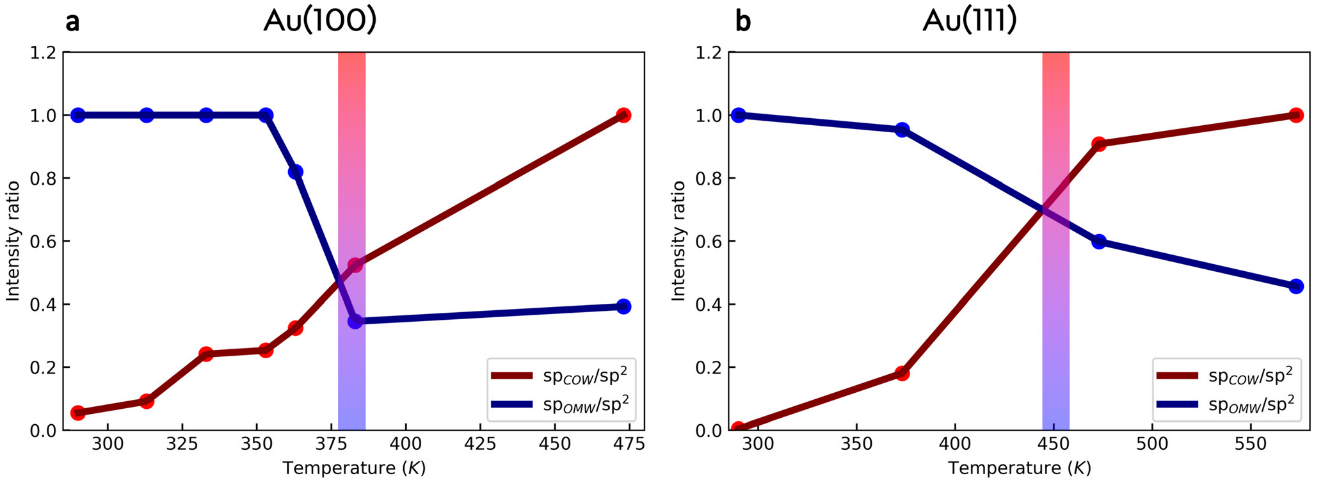

Fig. 8 Intensity ratio between the sp$_{\text{COW}}$ peak, in red (the sp$_{\text{OMW}}$ peak, in blue) and the sp^2 peak for the MWs domains as a function of the applied annealing temperature, on Au(100) (a) and Au(111) (b). Normalization by sp^2 peak was adopted due to its constant intensity throughout the whole temperature-dependent experiment. The coloured vertical bands indicate the temperature at which the inversion between the sp$_{\text{COW}}$/sp^2 and the sp$_{\text{OMW}}$/sp^2 contributions takes place, *i.e.*, about 373 K on Au(100) and about 473 K on Au(111).

Based on the analysis of the Raman results, we were able to compare the OMW-to-COW transition efficiency on Au(100) and Au(111) as a function of the annealing temperature. Fig. 8a and b shows the trend of the intensity ratio between the sp_{COW} peak, in red (the sp_{OMW} peak, in blue) and the sp^2 peak for the MWs domains as a function of the applied annealing temperature, on Au(100) and Au(111), respectively. It can be observed that upon mild annealing conditions, the main contribution is the sp_{OMW}/sp^2, in agreement with the prominent presence of the organometallic phase. By increasing the annealing temperature, the sp_{OMW}/sp^2 value decreases, simultaneously to the increase of the sp_{COW}/sp^2 one, according to the progressive removal of the gold adatoms and the simultaneously occurring homocoupling. After the inversion point, indicated by the coloured band in Fig. 8a and b, sp_{COW}/sp^2 overcomes sp_{OMW}/sp^2, in agreement with the prominent presence of the homocoupled phase. The inversion between sp_{COW}/sp^2 and sp_{OMW}/sp^2 is reached at about 373 K on Au(100) and 473 K on Au(111), demonstrating that the OMW-to-COW transition is more efficient on Au(100).

It is worth noting that the transition temperatures identified in Fig. 8 are the same that we extracted from the evolution of STM images (Fig. 5), further confirming the different efficiency of the process on the two surfaces.

Conclusions

We demonstrated the successful on-surface synthesis of 1,4-bBEB-based GDY MWs on Au(111) and Au(100). STM imaging, LEED experiments, and DFT calculations allowed for a comprehensive understanding of the atomic-scale structure and morphological evolution of the deposited wires on Au(100) and Au(111) upon the application of progressively higher annealing temperatures. *In situ* monitoring of their vibrational properties by Raman spectroscopy measurements, performed upon each annealing step, allowed us to confirm the STM-based assignment of the organometallic and covalent phases, whose spectral fingerprint was assessed for the first time, as well as the role of substrate orientation in affecting the OMW-to-COW transition efficiency.

These findings highlight the great potential of combining *in situ* Raman spectroscopy, STM imaging, and LEED to obtain an in-depth characterization of the morphological and vibrational properties of low dimensional carbon nanostructures. Moreover, it demonstrates the possibility to improve the controllability and efficiency of the Ullmann coupling by tuning the metal surface orientation. The knowledge gained from this study paves the way for further exploration of low dimensional carbon allotropes, as well as the potential development of novel functional materials based on graphdiyne structures.

Author contributions

A. C. designed and conducted the STM, LEED and Raman experiments, analyzed data, wrote the initial draft. P. D. and F. T. conducted the STM, LEED and Raman experiments and contributed to data analysis. S. A. conceived the theoretical modeling, performed the DFT calculations, analyzed the data and contributed to writing the initial draft. S. G. contributed to LT-STM imaging. A. O. B. synthesized the molecular precursor. G. O. and G. F. supported the analysis of the theoretical data. V. R. discussed Raman data analysis. S. M. contributed to the LT-STM experiments and analysis. A. L. B. and C. S. C. contributed in conceptualization, supervision and discussion of results. A. C. and S. A. contributed equally to this work and wrote the manuscript. All authors contributed to the revision and final discussion of the manuscript.

Conflicts of interest

There are no conflicts of interest to declare.

Data availability

Data for this article, including experimental STM images, Raman spectra and simulated structures are available at Zenodo at https://doi.org/10.5281/zenodo.17748647.

Supplementary information (SI): additional structural models, 2D FFT, STM images, LEED measurements and Raman spectra. See DOI: https://doi.org/10.1039/d5nr01968k.

Acknowledgements

A. C., V. R., A. L. B. and C. S. C acknowledge funding by: – Funder: project funded under the National Recovery and Resilience Plan (NRRP), Mission 4 Component 2 Investment 1.3 – Call for tender no. 341 of 15.03.2022 of Ministero dell'Universita' e della Ricerca (MUR); funded by the European Union NextGenerationEU – Award Number: project code PE0000021, Concession Decree No. 1561 of 11.10.2022 adopted by Ministero dell'Università e della Ricerca (MUR), CUP D43C22003090001, Project title "Network 4 Energy Sustainable Transition NEST". The authors also acknowledge funding from the European Research Council (ERC) under the European Union's Horizon 2020 research and innovation program ERC–Consolidator Grant (ERC CoG 2016 EspLORE grant agreement no. 724610, website: https://www.esplore.polimi.it). S. A., G. F. and G. O. acknowledge CINECA for the use of supercomputing facilities under the IscraC program (project DECANET – ID: HP10CN6MUU) and the project "TIME2QUEST" (Progetto di Iniziativa Specifica INFN). A. O. B. acknowledges support from the Ministero dell'Università e della Ricerca (MUR) and the University of Pavia through the program "Dipartimenti di Eccellenza 2023–2027". S. M. and S. G. acknowledge support from the Deutsche Forschungsgemeinschaft (DFG, German Research Foundation) – GRK 2861 (project number: 491865171).

References

1 G. Li, Y. Li, H. Liu, Y. Guo, Y. Li and D. Zhu, Architecture of graphdiyne nanoscale films, *Chem. Commun.*, 2010, **46**, 3256–3258.

2 R. Baughman, H. Eckhardt and M. Kertesz, Structure-property predictions for new planar forms of carbon: Layered phases containing sp2 and sp atoms, *J. Chem. Phys.*, 1987, **87**, 6687–6699.

3 A. Rabia, F. Tumino, A. Milani, V. Russo, A. Li Bassi, N. Bassi, A. Lucotti, S. Achilli, G. Fratesi, N. Manini, G. Onida, Q. Sun, W. Xu and C. S. Casari, Structural, electronic, and vibrational properties of a two-dimensional graphdiyne-like carbon nanonetwork synthesized on Au (111): implications for the engineering of sp-sp2 carbon nanostructures, *ACS Appl. Nano Mater.*, 2020, **3**, 12178–12187.

4 Y. Xue, Y. Li, J. Zhang, Z. Liu and Y. Zhao, 2D graphdiyne materials: challenges and opportunities in energy field, *Sci. China: Chem.*, 2018, **61**, 765–786.

5 C. Huang, S. Zhang, H. Liu, Y. Li, G. Cui and Y. Li, Graphdiyne for high capacity and long-life lithium storage, *Nano Energy*, 2015, **11**, 481–489.

6 X. Li, H. Zhang and L. Chi, On-Surface Synthesis of Graphyne-Based Nanostructures, *Adv. Mater.*, 2019, **31**, 1804087.

7 X. Gao, H. Liu, D. Wang and J. Zhang, Graphdiyne: synthesis, properties, and applications, *Chem. Soc. Rev.*, 2019, **48**, 908–936.

8 Y. Li, L. Xu, H. Liu and Y. Li, Graphdiyne and graphyne: from theoretical predictions to practical construction, *Chem. Soc. Rev.*, 2014, **43**, 2572–2586.

9 C. S. Casari, M. Tommasini, R. R. Tykwinski and A. Milani, Carbon-atom wires: 1D systems with tunable properties, *Nanoscale*, 2016, **8**, 4414–4435.

10 P. Serafini, A. Milani, M. Tommasini, C. Castiglioni and C. S. Casari, Raman and IR spectra of graphdiyne nanoribbons, *Phys. Rev. Mater.*, 2020, **4**, 014001.

11 P. Serafini, A. Milani, D. M. Proserpio and C. S. Casari, Designing all graphdiyne materials as graphene derivatives: topologically driven modulation of electronic properties, *J. Phys. Chem. C*, 2021, **125**, 18456–18466.

12 W. Zhao, F. Haag, I. Piquero-Zulaica, Z. M. Abd El-Fattah, P. Pendem, P. Vezzoni Vicente, Y.-Q. Zhang, N. Cao, A. P. Seitsonen, F. Allegretti, *et al.*, Transmetalation in Surface-Confined Single-Layer Organometallic Networks with Alkynyl–Metal–Alkynyl Linkages, *ACS Nano*, 2024, **18**, 20157–20166.

13 Z. Yang, T. Sander, J. Gebhardt, T. A. Schaub, J. Schonamsgruber, H. R. Soni, A. Gorling, M. Kivala and S. Maier, Metalated graphyne-based networks as two-dimensional materials: crystallization, topological defects, delocalized electronic states, and site-specific doping, *ACS Nano*, 2020, **14**, 16887–16896.

14 Z. Jia, Y. Li, Z. Zuo, H. Liu, C. Huang and Y. Li, Synthesis and Properties of 2D Carbon Graphdiyne, *Acc. Chem. Res.*, 2017, **50**, 2470–2478.

15 H. Yu, Y. Xue and Y. Li, Graphdiyne and its assembly architectures: synthesis, functionalization, and applications, *Adv. Mater.*, 2019, **31**, 1803101.

16 Q. Yue, S. Chang, J. Kang, S. Qin and J. Li, Mechanical and electronic properties of graphyne and its family under elastic strain: theoretical predictions, *J. Phys. Chem. C*, 2013, **117**, 14804–14811.

17 L. Pan, L. Zhang, B. Song, S. Du and H.-J. Gao, Graphyne- and graphdiyne-based nanoribbons: density functional theory calculations of electronic structures, *Appl. Phys. Lett.*, 2011, **98**, 173102.

18 H. Bai, Y. Zhu, W. Qiao and Y. Huang, Structures, stabilities and electronic properties of graphdiyne nanoribbons, *RSC Adv.*, 2011, **1**, 768–775.

19 J. Kang, F. Wu and J. Li, Modulating the bandgaps of graphdiyne nanoribbons by transverse electric fields, *J. Phys.: Condens. Matter*, 2012, **24**, 165301.

20 H. Bu, M. Zhao, H. Zhang, X. Wang, Y. Xi and Z. Wang, Isoelectronic doping of graphdiyne with boron and nitrogen: stable configurations and band gap modification, *J. Phys. Chem. A*, 2012, **116**, 3934–3939.

21 J. Zhou, K. Lv, Q. Wang, X. Chen, Q. Sun and P. Jena, Electronic structures and bonding of graphyne sheet and its BN analog, *J. Phys. Chem. A*, 2011, **134**, 174701.

22 S. Yang and M. Kertesz, Linear Cn clusters: are they acetylenic or cumulenic?, *J. Phys. Chem. A*, 2008, **112**, 146–151.

23 Y. Gao, Y. Hou, F. Gordillo Gámez, M. J. Ferguson, J. Casado and R. R. Tykwinski, The loss of endgroup effects in long pyridyl-endcapped oligoynes on the way to carbyne, *Nat. Chem.*, 2020, **12**, 1143–1149.

24 F. Cataldo, O. Ursini, A. Milani and C. S. Casari, One-pot synthesis and characterization of polyynes end-capped by biphenyl groups (α,ω -biphenylpolyynes), *Carbon*, 2018, **126**, 232–240.

25 Y. Zhu, H. Bai and Y. Huang, Electronic property and charge carrier mobility of extended nanowires built from narrow graphene nanoribbon and atomic carbon chain, *Synth. Met.*, 2015, **204**, 57–64.

26 Y. Zhu, H. Bai and Y. Huang, Electronic Property Modulation of One-Dimensional Extended Graphdiyne Nanowires from a First-Principle Crystal Orbital View, *ChemistryOpen*, 2016, **5**, 78–87.

27 A. Rabia, F. Tumino, A. Milani, V. Russo, A. Li Bassi, S. Achilli, G. Fratesi, G. Onida, N. Manini, Q. Sun, W. Xu and C. S. Casari, Scanning tunneling microscopy and Raman spectroscopy of polymeric sp–sp2 carbon atomic wires synthesized on the Au (111) surface, *Nanoscale*, 2019, **11**, 18191–18200.

28 Z. Zanolli, G. Onida and J.-C. Charlier, Quantum spin transport in carbon chains, *ACS Nano*, 2010, **4**, 5174–5180.

29 Q. Sun, L. Cai, H. Ma, C. Yuan and W. Xu, Dehalogenative homocoupling of terminal alkynyl bromides on Au (111): incorporation of acetylenic scaffolding into surface nanostructures, *ACS Nano*, 2016, **10**, 7023–7030.

30 J. Hu, Z. Liang, K. Shen, H. Sun, Z. Jiang and F. Song, Recent Progress in the Fabrication of Low Dimensional

Nanostructures via Surface-Assisted Transforming and Coupling, *J. Nanomater.*, 2017, **2017**, 4796538.

31 J. Bjork, F. Hanke and S. Stafstrom, Mechanisms of halogen-based covalent self-assembly on metal surfaces, *J. Am. Chem. Soc.*, 2013, **135**, 5768–5775.

32 J. Björk, Reaction mechanisms for on-surface synthesis of covalent nanostructures, *J. Phys.: Condens. Matter*, 2016, **28**, 083002.

33 X. Zhou, F. Bebensee, Q. Shen, R. Bebensee, F. Cheng, Y. He, H. Su, W. Chen, G. Q. Xu, F. Besenbacher, T. R. Linderoth and K. Wu, On-surface synthesis approach to preparing one-dimensional organometallic and poly-p-phenylene chains, *Mater. Chem. Front.*, 2017, **1**, 119–127.

34 F. Sedona, M. M. S. Fakhrabadi, S. Carlotto, E. Mohebbi, F. De Boni, S. Casalini, M. Casarin and M. Sambi, On-surface synthesis of extended linear graphyne molecular wires by protecting the alkynyl group, *Phys. Chem. Chem. Phys.*, 2020, **22**, 12180–12186.

35 F. De Boni, R. Pilot, A. Milani, V. V. Ivanovskaya, R. J. Abraham, S. Casalini, D. Pedron, C. S. Casari, M. Sambi and F. Sedona, Structure and vibrational properties of 1D molecular wires: from graphene to graphdiyne, *Nanoscale*, 2024, **16**, 11211–11222.

36 H. Li, Y. Wang, B. Yang, H. Zhang, M. Xie and L. Chi, Theoretical Investigation on the Initial Reaction Mechanism of Hexaethynylbenzene on Au (111) Surface, *J. Phys. Chem. A*, 2024, **128**, 7536–7545.

37 J. Wang, K. Niu, H. Zhu, C. Xu, C. Deng, W. Zhao, P. Huang, H. Lin, D. Li, J. Rosen, P. Liu, F. Allegretti, J. V. Barth, B. Yang, J. Björk, Q. Li and L. Chi, Universal inter-molecular radical transfer reactions on metal surfaces, *Nat. Commun.*, 2024, **15**, 3030.

38 F. Klappenberger, R. Hellwig, P. Du, T. Paintner, M. Uphoff, L. Zhang, T. Lin, B. A. Moghanaki, M. Paszkiewicz, I. Vobornik, J. Fujii, O. Fuhr, Y.-Q. Zhang, F. Allegretti, M. Ruben and J. V. Barth, Functionalized graphdiyne nanowires: on-surface synthesis and assessment of band structure, flexibility, and information storage potential, *Small*, 2018, **14**, 1704321.

39 S. Achilli, A. Milani, G. Fratesi, F. Tumino, N. Manini, G. Onida and C. S. Casari, Graphdiynes interacting with metal surfaces: first-principles electronic and vibrational properties, *2D Mater.*, 2021, **8**, 044014.

40 J. Eichhorn, W. M. Heckl and M. Lackinger, On-surface polymerization of 1,4-diethynylbenzene on Cu (111), *Chem. Commun.*, 2013, **49**, 2900–2902.

41 R. R. Tykwinski, W. Chalifoux, S. Eisler, A. Lucotti, M. Tommasini, D. Fazzi, M. Del Zoppo and G. Zerbi, Toward carbyne: Synthesis and stability of really long polyynes, *Pure Appl. Chem.*, 2010, **82**, 891–904.

42 F. Cataldo, Stability of polyynes in air and their degradation by ozonolysis, *Polym. Degrad. Stab.*, 2006, **91**, 317–323.

43 X. Li, H. Ge, Y. Gao, F. Yang, F. Kang, R. Xue, L. Yan, S. Du, W. Xu, H. Zhang and L. Chi, Scanning Tunneling Spectroscopy Investigation of Au-bis-acetylide Networks on Au (111): The Influence of Metal–Organic Hybridization, *J. Phys. Chem. Lett.*, 2024, **15**, 4593–4601.

44 Y.-Q. Zhang, T. Paintner, R. Hellwig, F. Haag, F. Allegretti, P. Feulner, S. Klyatskaya, M. Ruben, A. P. Seitsonen, J. V. Barth and F. Klappenberger, Synthesizing highly regular single-layer alkynyl–silver networks at the micrometer scale via gas-mediated surface reaction, *J. Am. Chem. Soc.*, 2019, **141**, 5087–5091.

45 C. Huang, Y. Li, N. Wang, Y. Xue, Z. Zuo, H. Liu and Y. Li, Progress in research into 2D graphdiyne-based materials, *Chem. Rev.*, 2018, **118**, 7744–7803.

46 Y. Liu, F. Gao, P. Cheng, L. Chen, S. Klyatskaya, M. Ruben, J. Rosen, J. V. Barth, J. Björk, K. Wu and Y.-Q. Zhang, Unraveling Enyne Bonding via Dehydrogenation–Hydrogenation Processes in On-Surface Synthesis with Terminal Alkynes, *Adv. Mater. Interfaces*, 2024, **11**, 2400222.

47 M. Abadia, I. Piquero-Zulaica, J. Brede, A. Verdini, L. Floreano, J. V. Barth, J. Lobo-Checa, M. Corso and C. Rogero, Enhancing Haloarene Coupling Reaction Efficiency on an Oxide Surface by Metal Atom Addition, *Nano Lett.*, 2024, **24**, 1923–1930.

48 C. S. Casari and A. Milani, Carbyne: from the elusive allotrope to stable carbon atom wires, *Mrs Commun.*, 2018, **8**, 207–219.

49 J. Zhang, J. Z. Sun, A. Qin and B. Z. Tang, Transition-metal-free polymerization of bromoalkynes and phenols, *Macromolecules*, 2019, **52**, 2949–2955.

50 S. Kerfriden, A. Nahle, S. Campbell, F. Walsh and J. Smith, The electrochemical etching of tungsten STM tips, *Electrochim. Acta*, 1998, **43**, 1939–1944.

51 D. Nečas and P. Klapetek, Gwyddion: an open-source software for SPM data analysis, *Open Phys. J.*, 2012, **10**, 181–188.

52 M. Wojdyr, Fityk: a general-purpose peak fitting program, *J. Appl. Crystallogr.*, 2010, **43**, 1126–1128.

53 J. P. Perdew, K. Burke and M. Ernzerhof, Generalized Gradient Approximation Made Simple, *Phys. Rev. Lett.*, 1996, **77**, 3865–3868.

54 J. M. Soler, E. Artacho, J. D. Gale, A. García, J. Junquera, P. Ordejón and D. Sánchez-Portal, The SIESTA Method for *Ab Initio* Order-N Materials Simulation, *J. Phys.: Condens. Matter*, 2002, **14**, 2745.

55 S. Baroni, S. De Gironcoli, A. Dal Corso and P. Giannozzi, Phonons and related crystal properties from density-functional perturbation theory, *Rev. Mod. Phys.*, 2001, **73**, 515–562.

56 P. Giannozzi, O. Andreussi, T. Brumme, O. Bunau, M. B. Nardelli, M. Calandra, R. Car, C. Cavazzoni, D. Ceresoli, M. Cococcioni, N. Colonna, I. Carnimeo, A. D. Corso, S. de Gironcoli, P. Delugas, R. A. D. Jr, A. Ferretti, A. Floris, G. Fratesi, G. Fugallo, *et al.*, Advanced capabilities for materials modelling with QUANTUM ESPRESSO, *J. Phys.: Condens. Matter*, 2017, **29**, 465901.

57 P. Giannozzi, S. Baroni, N. Bonini, M. Calandra, R. Car, C. Cavazzoni, D. Ceresoli, G. L. Chiarotti, M. Cococcioni, I. Dabo, A. Dal Corso, S. de Gironcoli, S. Fabris, G. Fratesi, R. Gebauer, U. Gerstmann, C. Gougoussis, A. Kokalj, M. Lazzeri, L. Martin-Samos, *et al.*, Quantum ESPRESSO: a

modular and open-source software project for quantum simulations of materials, *J. Phys.: Condens. Matter*, 2009, **21**, 395502.

58 S. Grimme, Semiempirical GGA-Type Density Functional Constructed with a Long-Range Dispersion Correction, *J. Comput. Chem.*, 2006, **27**, 1787–1799.

59 J. Tersoff and D. R. Hamann, Theory of the Scanning Tunneling Microscope, *Phys. Rev. B:Condens. Matter Mater. Phys.*, 1985, **31**, 805.

60 A. D. Corso, Pseudopotentials periodic table: From H to Pu, *Comput. Mater.*, 2014, **95**, 337.

61 N. Tao and S. Lindsay, In situ scanning tunneling microscopy study of iodine and bromine adsorption on gold (111) under potential control, *J. Phys. Chem.*, 1992, **96**, 5213–5217.

62 H. Zhang, H. Lin, L. Chen, Y. Zagranyarski, N. Aghdassi, S. Duhm, Q. Li, D. Zhong, Y. Li, K. Mullen, H. Fuchs and L. Chi, On-surface synthesis of rylene-type graphene nanoribbons, *J. Am. Chem. Soc.*, 2015, **137**, 4022–4025.

63 K. Sun, T. Nishiuchi, K. Sahara, T. Kubo, A. S. Foster and S. Kawai, Low-temperature removal of dissociated bromine by silicon atoms for an on-surface Ullmann reaction, *J. Phys. Chem. C*, 2020, **124**, 19675–19680.

64 P. Dobson, The surface structure of gold: The origin of abnormalities in the outer atomic layers, *Gold Bull.*, 1974, **7**, 15–19.

65 Y. Jiang, X. Liang, S. Ren, C.-L. Chen, L.-J. Fan, Y.-W. Yang, J.-M. Tang and D.-A. Luh, The growth of sulfur adlayers on Au (100), *J. Chem. Phys.*, 2015, **142**, 064708.

66 S. Bengió, V. Navarro, M. González-Barrio, R. Cortés, I. Vobornik, E. G. Michel and A. Mascaraque, Electronic structure of reconstructed Au (100): Two-dimensional and one-dimensional surface states, *Phys. Rev. B*, 2012, **86**, 045426.

67 F. De Boni, G. Merlin, F. Sedona, S. Casalini, M. M. Seyyed Fakhrabadi and M. Sambi, Templating Effect of Different Low-Miller-Index Gold Surfaces on the Bottom-Up Growth of Graphene Nanoribbons, *ACS Appl. Nano Mater.*, 2020, **3**, 11497–11509.

68 E. Cinquanta, L. Ravagnan, I. E. Castelli, F. Cataldo, N. Manini, G. Onida and P. Milani, Vibrational characterization of dinaphthylpolyynes: A model system for the sudy of end-capped sp carbon chains, *J. Chem. Phys.*, 2011, **135**, 194501.

69 L. Ravagnan, N. Manini, E. Cinquanta, G. Onida, D. Sangalli, C. Motta, M. Devetta, A. Bordoni, P. Piseri and P. Milani, Effect of axial torsion on sp carbon atomic wires, *Phys. Rev. Lett.*, 2009, **102**, 24550.